



日本原子力研究開発機構機関リポジトリ  
Japan Atomic Energy Agency Institutional Repository

Title	Development of spin-contrast-variation neutron powder diffractometry for extracting the structure factor of hydrogen atoms
Author(s)	Miura Daisuke, Kumada Takayuki, Sekine Yurina, Motokawa Ryuhei, Nakagawa Hiroshi, Oba Yojiro, Ohara Takashi, Takata Shinichi, Hiroi Kosuke, Morikawa Toshiaki, Kawamura Yukihiro, Oishi Kazuki, Suzuki Junichi, Miyachi Yoshiyuki, Iwata Takahiro
Citation	Journal of Applied Crystallography, 54(2), p.454-460
Text Version	Preprint
URL	<a href="https://jopss.jaea.go.jp/search/servlet/search?5070754">https://jopss.jaea.go.jp/search/servlet/search?5070754</a>
DOI	<a href="https://doi.org/10.1107/S1600576721000303">https://doi.org/10.1107/S1600576721000303</a>
Right	© International Union of Crystallography

# Development of spin-contrast-variation neutron powder diffractometry for extracting the structure factor of hydrogen atoms

DAISUKE MIURA,<sup>a,b</sup> TAKAYUKI KUMADA,<sup>b\*</sup> YURINA SEKINE,<sup>b</sup>  
RYUHEI MOTOKAWA,<sup>b</sup> HIROSHI NAKAGAWA,<sup>b</sup> YOJIRO OBA,<sup>b</sup> TAKASHI OHHARA,<sup>c</sup>  
SHIN-ICHI TAKATA,<sup>c</sup> KOSUKE HIROI,<sup>c</sup> TOSHIAKI MORIKAWA,<sup>d</sup>  
YUKIHIKO KAWAMURA,<sup>d</sup> KAZUKI OHISHI,<sup>d</sup> JUN-ICHI SUZUKI,<sup>d</sup>  
YOSHIYUKI MIYACHI<sup>a</sup> AND TAKAHIRO IWATA<sup>a</sup>

<sup>a</sup>*Department of Physics, Yamagata University, Yamagata, Yamagata 990-8560, Japan,* <sup>b</sup>*Materials Sciences Research Center, Japan Atomic Energy Agency (JAEA), Tokai, Ibaraki 319-1195, Japan,* <sup>c</sup>*Japan Proton Accelerator Research Complex (J-PARC) Center, JAEA, Tokai, Ibaraki 319-1195 Japan,* and <sup>d</sup>*Neutron Science and Technology Center, Comprehensive Research Organization for Science and Society (CROSS), Tokai, Ibaraki 319-1106, Japan. E-mail: kumada.takayuki@jaea.go.jp*

**spin-contrast-variation; neutron powder diffractometry; dynamic nuclear polarization**

## Abstract

We developed a spin-contrast-variation neutron powder diffractometry technique that extracts the structure factor of hydrogen atoms, namely, the contribution of hydrogen atoms to a crystal's structure factor. Crystals of L-glutamic acid were dispersed in a d-polystyrene matrix containing 4-methacryloyloxy-2,2,6,6,-tetramethyl-1-piperidinyloxy

(TEMPO methacrylate) to polarize their proton spins dynamically. The intensities of the diffraction peaks of the sample changed according to the proton polarization, and the structure factor of the hydrogen atoms was extracted from the proton-polarization-dependent intensities. This technique is expected to enable analyses of the structures of hydrogen-containing materials that are difficult to determine with conventional powder diffractometry.

## 1. Introduction

Neutron scattering and X-ray scattering are powerful techniques for analyzing crystalline structures. In particular, neutron scattering is better suited than X-ray scattering for studying the structures of hydrogen-containing materials. The neutron coherent scattering cross section of hydrogen is comparable with those of other elements, whereas the X-ray cross section of hydrogen is much smaller. Hydrogen-containing materials are usually deuterated for neutron-scattering measurements because deuterium has a larger coherent scattering length and a smaller incoherent scattering length than those of hydrogen. However, preparing such deuterated samples is difficult and in some cases impossible.

To overcome this difficulty, an alternative technique known as spin contrast variation (SCV) using polarized neutrons and protons (Knop *et al.*, 1989; Knop *et al.*, 1991; Knop *et al.*, 1992; Stuhrmann, 2004) was developed. The coherent polarized neutron scattering length of hydrogen,  $b_{\text{H}}$ , varies according to the proton spin polarization  $P_{\text{H}}$  with respect to the neutron spin direction as

$$b_{\text{H}} = b_{\text{H}0} + \Delta b_{\text{H}} P_{\text{H}} , \quad (1)$$

with  $b_{\text{H}0} = -3.74$  fm and  $\Delta b_{\text{H}} = 14.56$  fm (Sears, 1992). In contrast, the corresponding polarization dependence is negligibly small in other elements. Combined with small-angle neutron scattering, SCV has been used to elucidate the nanostructures of soft

composite materials (Knop *et al.*, 1989; Knop *et al.*, 1991; Knop *et al.*, 1992; van den Brandt *et al.*, 2002; Noda *et al.*, 2016), and SCV neutron reflectivity was developed recently to determine the surface and interfacial structures of multilayered films (Kumada *et al.*, 2019).

In crystallography, SCV provides the structure factor of hydrogen atoms, namely the contribution of hydrogen atoms to a crystal's structure factor. Fig. 1 shows the crystal structure of the  $\beta$  phase of L-glutamic acid as an example. SCV neutron diffractometry can focus on hydrogen from the  $P_{\text{H}}$ -dependent diffraction profiles, whereas conventional neutron diffractometry cannot distinguish between hydrogen and other elements. However, SCV has been relatively underused in diffractometry to date because the polarization technique is severely limited regarding crystalline samples. In SCV, the sample is hyperpolarized by dynamic nuclear polarization (DNP), which transfers spin polarization from electrons to protons using microwaves with a frequency close to electron paramagnetic resonance (EPR) (Abragam & Goldman, 1978). Here, doping of the electron spins, which act as a polarizing agent, is a key factor of DNP. Glassy samples are doped with polarizing agents such as 2,2,6,6-tetramethyl-1-piperidinyloxy (TEMPO) stable free radicals, while rubbery polymers are permeated with vaporized TEMPO (van den Brandt *et al.*, 1995). However, crystalline samples generally can be neither doped nor permeated with such stable radicals.

In the long history of experiments in nuclear physics, crystalline samples of several types have been dynamically polarized. Proton polarization of more than 95% was achieved in  $\text{NH}_3$  and  $^7\text{LiH}$  crystals, where the polarizing agents were generated by electron-beam irradiation (Niinikoski & Rieubland, 1979; Roinel *et al.*, 1978). Proton polarization of more than 70% was obtained in  $\text{La}_2\text{Mg}_3(\text{NO}_3)_{12}\cdot 24\text{H}_2\text{O}$  (LMN) using  $\text{Nd}^{3+}$  paramagnetic centers that were partially substituted for  $\text{La}^{3+}$  (Abragam *et al.*, 1962; Schmugge & Jeffries, 1965), and it has been shown that changing the proton

polarization changes the polarized neutron diffraction intensity of LMN (Hayter *et al.*, 1974; Piegsa *et al.*, 2012). However, these doping techniques are severely limited. Electron-beam irradiation is applicable only when the EPR linewidth of the unpaired electrons generated by the radiolysis is narrow enough for DNP (Goertz *et al.*, 2004). Also, because the EPR patterns of paramagnetic centers such as  $\text{Nd}^{3+}$  differ according to the sample (Borghini, 1966), the best ionic species must be found for each sample. Therefore, neither irradiation nor ion substitution is suited to studying the structure of crystalline samples when various samples arrive at a neutron facility and must be polarized. These technical difficulties have prevented SCV from being extended to neutron diffractometry, except for protein crystals that can be polarized by doping TEMPO or hydroxy-TEMPO into swollen glassy solvents (Zhao *et al.*, 2013; Pierce, 2017; Tanaka *et al.*, 2018; Pierce *et al.*, 2020).

Meanwhile, a versatile DNP technique for crystalline samples was developed for solid-state nuclear magnetic resonance experiments (Rossini *et al.*, 2012). In this technique, dispersion medias doped with free radicals derivatives are impregnated with milled molecular microcrystals to polarize the latter via spin diffusion from the dynamically polarized media. The advantage of this technique, known as relayed DNP, is that the crystalline samples are polarized even though crystalline domains are not doped with free radicals. Thus, this technique can polarize any crystalline samples as long as the growth rate of nuclear polarization due to microwave excitation is higher than the longitudinal nuclear spin relaxation rate. Recently, we carried out DNP measurements of  $\text{LaF}_3$  nanocrystals dispersed in TEMPO-containing ethanol at 2.5 T and 0.9 K (Miura *et al.*, 2019), which are close to the conditions of our SCV experiments (Kumada *et al.*, 2009). The polarization of  $^{19}\text{F}$  nuclei, the magnetic moment of which is very close to that of protons, increased to 13.5% (unpublished), which indicates that relayed DNP can polarize protons sufficiently for SCV diffractometry measurements.

In the present study, we use relayed DNP to develop a versatile SCV neutron powder diffraction (SCV-NPD) technique. The diffraction intensities of L-glutamic acid (LGA) change with  $P_H$  differently for each peak, and the structure factor of hydrogen is extracted from the  $P_H$ -dependent intensity.

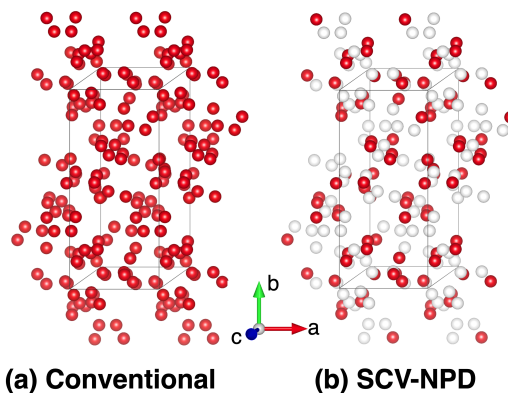


Fig. 1. Crystal structure of  $\beta$  phase of L-glutamic acid: (a) conventional diffractometry detects all elements (red spheres); (b) spin-contrast-variation neutron powder diffraction (SCV-NPD) detects only hydrogen (red spheres) and not other elements (white spheres). The box drawn with solid lines indicates a unit cell.

## 2. Experiment

### 2.1. Sample preparation

The samples comprised LGA powder in the  $\beta$  phase and dispersed in deuterated polystyrene doped with 25 mM of 4-methacryloyloxy-TEMPO (TEMPO methacrylate), prepared according to the following scheme. First, 500 mg of LGA (56-86-0; Fujifilm Wako Pure Chemical Corp., Japan) were milled with a pestle and a mortar into a micropowder. The micropowder was impregnated with 15 mL of cyclohexane and dispersed using an ultrasonic wave (Qsonica Q500; WakenBtech) for 30 min. Then, 1 g of deuterated polystyrene (polymer source, p2015-dPS,  $M_w = 970$ ,  $M_w/M_n = 1.10$ ) and TEMPO methacrylate (730297, Sigma-Aldrich,) were dissolved in cyclohexane, which was later evaporated in a vacuum oven at 110°C for 12 h to form submillimeter-thick

sheets. It was confirmed by X-ray diffractometry (MiniFlex600; Rigaku) that the  $\beta$  phase of LGA was maintained even after the milling, impregnation, and heating. Four sheets with a total thickness of approximately 3 mm were stacked and set in a sample cell made of aluminum for neutron diffraction measurements.

## 2.2. Neutron diffraction measurement

The SCV-NPD experiment was performed by placing our DNP apparatus in the small and wide-angle neutron scattering instrument TAIKAN (BL15) (Takata *et al.*, 2015) in the Materials and Life Science Experimental Facility (MLF) of the Japan Proton Accelerator Research Complex (J-PARC). Fig. 2 shows the instrumental configuration. Pulsed neutrons from a mercury spallation target were polarized antiparallel to the beam direction with the neutron spin polarizer, spin-flipped with the spin flipper if needed, diffracted from the proton-polarized sample in the DNP apparatus, and detected with the middle-angle and backward detectors. The DNP apparatus comprised a liquid  $^4\text{He}$  cryostat that cooled the sample down to 1.2 K by pumping with a scroll pump (NeoDry60E; Kashiyama) and two booster pumps (SMB-C06 and SMB-C25; Shinko Seiki), a Helmholtz magnet (JMTC-3.5T/50/SP; JASTEC) that generated a magnetic field of 3.33 T, a microwave oscillator that generated a frequency of 93.9 GHz, and a microwave amplifier (AMP-10-01300; Millitech) (Kumada *et al.*, 2009). The direction of the proton polarization of the sample was maintained parallel to the magnetic field. The sign of  $P_{\text{H}}$  was switched by controlling the direction of the neutron spin with the spin flipper. When the sample was unpolarized, the magnetic field was set to zero. The magnitude of  $P_{\text{H}}$  was determined to be 16% from the ratio between the neutron transmissions of the polarized and unpolarized samples following the procedure described in (Noda *et al.*, 2011). The opening angle of the neutron window was so small that the DNP apparatus was rotated by  $19^\circ$  from

the direction of the incident neutrons to cover values of the scattering angle  $2\theta$  in the ranges of  $14\text{--}27^\circ$  and  $144\text{--}159^\circ$  with the middle-angle and backward detectors, respectively. Although the overall range of  $2\theta$  was severely limited, time-of-flight measurement with neutron wavelength  $\lambda$  from 1.6 to 7.5 Å offered seamless cover of the magnitude of the scattering vector, namely

$$Q = \frac{4\pi \sin \theta}{\lambda}, \quad (2)$$

from 0.4 to 1.6 Å<sup>-1</sup> and from 1.6 to 7.5 Å<sup>-1</sup> with the middle-angle and backward detectors, respectively. The scattering from a positively polarized sample, a negatively polarized one, and an unpolarized one was accumulated for 5 h in each case. From those data were subtracted the incoherent scattering of the sample, the coherent scattering of the deuterated polystyrene, and the scattering of the air, which appear as the broad spectra over the diffraction peaks in Fig.S2.

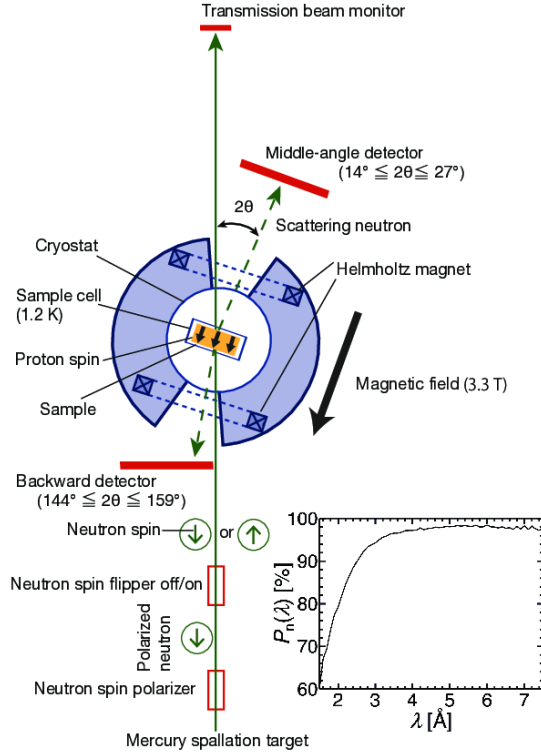


Fig. 2. Instrumental configuration of SCV-NPD measurements at TAIKAN. The inset shows the  $\lambda$  dependence of the neutron polarization.

### 2.3. Correction of scattering intensity

The observed neutron-scattering intensity  $I_{\text{obs}}^{\pm}(Q, |P_{\text{H}}|)$  is the sum of the intensities for different  $\lambda$ , namely

$$I_{\text{obs}}^{\pm}(Q, |P_{\text{H}}|) = \sum_{\lambda} I_{\text{obs},\lambda}^{\pm}(Q, |P_{\text{H}}|) , \quad (3)$$

where the superscript + or – indicates that the neutron polarization is parallel or antiparallel, respectively, to the proton polarization. Because the neutron polarization  $p_{\text{n}}(\lambda)$  varies with  $\lambda$  (see the inset of Fig. 2), we corrected  $I_{\text{obs}}^{\pm}(Q, |P_{\text{H}}|)$  to the intensity corresponding to  $p_{\text{n}}(\lambda) = 100\%$ , namely  $I(Q, P_{\text{H}})$ , as follows:

$$I(Q, P_{\text{H}}) = \sum_{\lambda} I_{\lambda}(Q, P_{\text{H}}) \quad (4)$$

with

$$I_{\lambda}(Q, P_{\text{H}}) = \frac{I_{\text{obs},\lambda}^{\pm}(Q, |P_{\text{H}}|) + I_{\text{obs},\lambda}^{\mp}(Q, |P_{\text{H}}|)}{2} + \frac{I_{\text{obs},\lambda}^{\pm}(Q, |P_{\text{H}}|) - I_{\text{obs},\lambda}^{\mp}(Q, |P_{\text{H}}|)}{2p_{\text{n}}(\lambda)} . \quad (5)$$

As shown in Fig.S1, the differences between  $I_{\text{obs}}^{\pm}(Q, |P_{\text{H}}|)$  and  $I(Q, P_{\text{H}})$  are not negligible, particularly around  $Q = 1.4 \text{ \AA}^{-1}$  where scattering neutrons with  $p_{\text{n}}(\lambda)$  less than 80% were measured.

#### 2.4. Calculation of crystal structure factor

The crystal structure factor

$$F(\mathbf{Q}, P_{\text{H}}) = \sum_j b_j e^{i\mathbf{Q} \cdot \mathbf{r}_j} \quad (6)$$

with scattering length  $b_j$  and position vector  $\mathbf{r}_j$  was calculated by importing the crystallographic information file (CIF) (Dunitz & Schweizer, 1995) of the  $\beta$  phase of LGA from the Crystallography Open Database (COD) (Downs & Hall-Wallace, 2003; Gražulis *et al.*, 2009; Gražulis *et al.*, 2012) to the Visualization for Electronic and Structural Analysis (VESTA) program (Momma & Izumi, 2011). However, because VESTA does not support the calculation of proton-polarized samples, the hydrogen scattering length was changed manually by adjusting the occupancy at hydrogen sites in the CIF data to calculate  $F(\mathbf{Q}, P_{\text{H}} \neq 0\%)$ . Note that the Debye–Waller factor of each atom was set to unity and that the lattice constants were reduced isotropically by 0.3% from the CIF data to reproduce the position of the diffraction peak at  $P_{\text{H}} = 0\%$  because of cryo-shrinking of the sample.

### 3. Results

Fig. 3(a) shows the SCV-NPD data for the  $\beta$  phase of the LGA samples in the range  $1.2 \leq Q \leq 2.6 \text{ \AA}^{-1}$  in which the diffraction peaks were observed clearly. How the peak intensities change with  $P_{\text{H}}$  differs for each value of  $Q$ . For example, the intensities of the peaks at  $Q = 1.27$  and  $1.46 \text{ \AA}^{-1}$  decrease with increasing  $P_{\text{H}}$ , whereas those at  $Q = 1.43$  and  $1.58 \text{ \AA}^{-1}$  increase, and the intensity at  $Q = 1.53 \text{ \AA}^{-1}$  is unchanged with  $P_{\text{H}}$ .

Fig. 3(b) shows the calculated peak intensities following

$$I(Q, P_H) = \frac{m(Q)}{Q^2} |F(\mathbf{Q}, P_H)|^2 \quad , \quad (7)$$

where  $m(Q)$  is the multiplicity and  $Q^{-2}$  is the Lorentz factor for the scattering from randomly oriented planes in plots of the differential scattering cross section versus  $Q$  (Shibayama *et al.*, 1989). How the peak intensity at each value of  $Q$  changes with  $P_H$  in Fig. 3(a) is consistent with that in Fig. 3(b).

The increase in peak intensity according to the proton polarization makes it possible to observe the peaks that are not visible at  $P_H = 0\%$ . For example, the peak at  $Q = 1.9 \text{ \AA}^{-1}$  in Fig. 3(a) was not seen with  $P_H = 0\%$ , but it was seen with  $P_H = 16\%$  thanks to the increase in peak intensity with  $P_H$ . The intensity change not only reveals the peaks that are hidden at  $P_H = 0\%$  but also helps to separate overlapping peaks. For instance, the mound structure observed around  $Q = 2.13 \text{ \AA}^{-1}$  with  $P_H = 0\%$  is asymmetric, suggesting that the sub-peak at  $Q = 2.11 \text{ \AA}^{-1}$  may be overlapped by the main peak at  $Q = 2.13 \text{ \AA}^{-1}$ ; it is difficult to prove its existence from only the structure with  $P_H = 0\%$ , but the structure with  $P_H = -16\%$  shows clearly that the sub-peak is overlapped. Moreover, overlapping of multiple peaks can be distinguished even when the difference in  $Q$  between adjacent peaks is smaller than the resolving power of the instruments. Looking at  $Q = 2.2 \text{ \AA}^{-1}$ , the peak position shifts very slightly to higher  $Q$  with  $P_H = 16\%$ , which can be interpreted as follows: as shown in Fig. 3(b), the intensity of one peak at  $Q$  slightly lower than the overlapped peak position decreases, but that of the other peak at higher  $Q$  increases with increasing  $P_H$ .

In the following section, we discuss why the change in intensity with  $P_H$  differs for each peak and how the structure factor of hydrogen atoms is extracted from the  $P_H$ -dependent peak intensities.

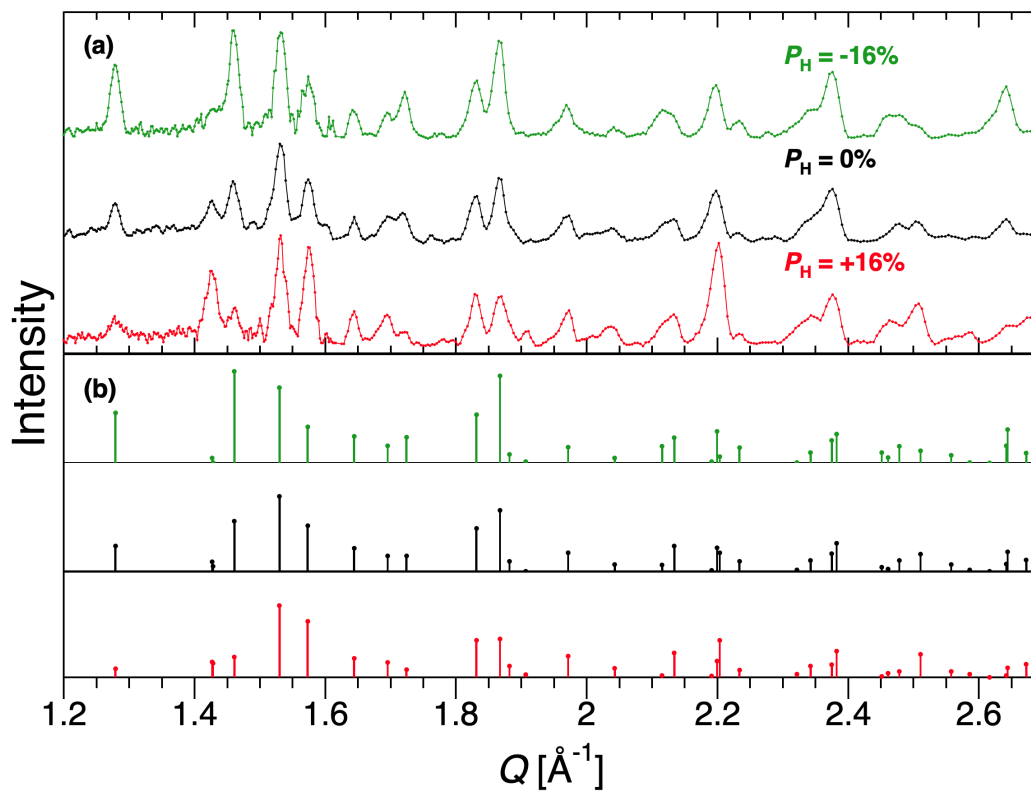


Fig. 3. (a) SCV-NPD data for  $\beta$  phase of LGA samples after subtracting the broad scattering in Fig.S2. (b) Calculated intensities of the peaks.

#### 4. Discussion

To discuss the  $P_H$  dependence of the intensity, we divide  $F(\mathbf{Q}, P_H)$  into two terms, namely, the structure factor  $F_H(\mathbf{Q})$  of hydrogen atoms at  $P_H = 0\%$  and the structure factor  $F_{\text{others}}(\mathbf{Q})$  of the other elements (C, N, and O in this case) as

$$F(\mathbf{Q}, P_H) = (1 - \kappa P_H)F_H(\mathbf{Q}) + F_{\text{others}}(\mathbf{Q}) . \quad (8)$$

Here,  $(1 - \kappa P_H)$  with  $\kappa = |\Delta b_H/b_{H0}| = 3.89$  in Eq. (1) is the ratio of the structure factor of hydrogen at  $P_H$  to that at  $P_H = 0\%$ . Substituting Eq. (8) into Eq. (7) gives

$$I(\mathbf{Q}, P_H) = \frac{m(\mathbf{Q})}{Q^2} \left( |F_{\text{others}}(\mathbf{Q})|^2 + (1 - \kappa P_H)^2 |F_H(\mathbf{Q})|^2 + 2(1 - \kappa P_H) \text{Re} [F_H(\mathbf{Q})F_{\text{others}}(\mathbf{Q})^*] \right) . \quad (9)$$

As shown in Fig. 4, the intensities of the peaks follow quadratic functions of  $P_H$  with different curvatures and vertex positions, which reflect  $|F_H(\mathbf{Q})|^2$  and  $\text{Re}[F_H(\mathbf{Q})F_{\text{others}}(\mathbf{Q})^*]$ , respectively. Ideally,  $|F_H(\mathbf{Q})|^2$  and  $\text{Re}[F_H(\mathbf{Q})F_{\text{others}}(\mathbf{Q})^*]$  would be determined by fitting Eq. (9) to the intensities of all the peaks at multiple values of  $P_H$ . However, such fitting is unrealistic because limited time prevents measurements at multiple values of  $P_H$  required for the fit.

Alternatively, we propose an analysis that extracts  $|F_H(\mathbf{Q})|^2$  and  $\text{Re}[F_H(\mathbf{Q})F_{\text{others}}(\mathbf{Q})^*]$  by subtracting Eq. (9) for only three different values of  $P_H$ . First,  $|F_{\text{others}}(\mathbf{Q})|^2$  is removed by subtraction, namely

$$\frac{1}{2} \frac{I(Q, -P_H) - I(Q, +P_H)}{2\kappa P_H} = \frac{m(Q)}{Q^2} \left\{ |F_H(\mathbf{Q})|^2 + \text{Re}[F_H(\mathbf{Q})F_{\text{others}}(\mathbf{Q})^*] \right\} . \quad (10)$$

The data shown by the blue single-line graph in Fig. 5(a) were obtained by substituting the intensities at  $P_H = \pm 16\%$  in Fig. 3 into  $I(Q, \pm P_H)$  in Eq. (10). Meanwhile, the orange filled-line graph is of  $|F_H(\mathbf{Q})|^2$  and  $\text{Re}[F_H(\mathbf{Q})F_{\text{others}}(\mathbf{Q})^*]$  of LGA and broadened using the resolving power of TAIKAN (Takata *et al.*, 2015). The experimental data and the calculation agree well regarding the peak positions and intensities, indicating that only the intensity change with  $P_H$  was picked up and the intensity related to  $F_H(\mathbf{Q})$  was extracted.

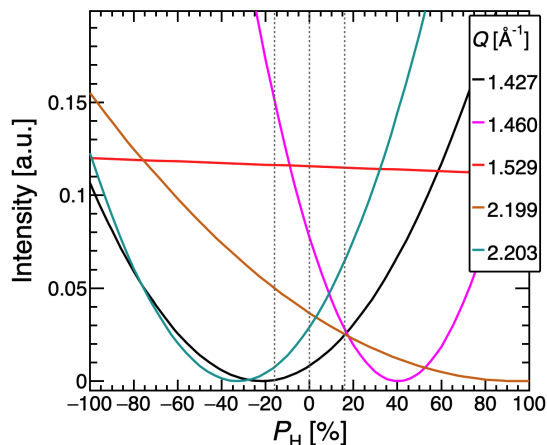


Fig. 4. Calculated intensities of several peaks as functions of  $P_H$ . The vertical dashed gray lines indicate the  $P_H$  values used in this experiment.

Second,  $|F_H(\mathbf{Q})|^2$  is obtained by further substituting the intensities at  $P_H = 0\%$  in Fig. 3 into

$$\frac{1}{2} \frac{I(Q, -P_H) + I(Q, +P_H) - 2I(Q, 0)}{(\kappa P_H)^2} = \frac{m(Q)}{Q^2} |F_H(\mathbf{Q})|^2 . \quad (11)$$

Fig. 5(b) compares the experimental data and the calculation corresponding to Eq. (11). The experimental data reproduce the calculated peaks, but the noise level is comparable with or even larger than the small peaks, especially those near  $Q = 1.6 \text{ \AA}^{-1}$ , which are located at the boundary of the high- and low- $Q$  detection limits for the middle-angle and backward detectors, respectively. The blue line graph in Fig. 5(b) shows the secondary differentiation against  $P_H$ , whereas that in Fig. 5(a) shows the primary differentiation. Therefore, it is more difficult to obtain Fig. 5(b) accurately than it is Fig. 5(a), except near the vertices of the parabolas in Fig. 4.

Third,  $\text{Re}[F_H(\mathbf{Q})F_{\text{others}}(\mathbf{Q})^*]$  in Fig. 5 is given by subtracting Eq. (11) from Eq. (10), namely

$$\begin{aligned} & \frac{1}{2} \left\{ \frac{I(Q, -P_H) - I(Q, +P_H)}{2\kappa P_H} - \frac{I(Q, -P_H) + I(Q, +P_H) - 2I(Q, 0)}{(\kappa P_H)^2} \right\} \\ & = \frac{m(Q)}{Q^2} \text{Re}[F_H(\mathbf{Q})F_{\text{others}}(\mathbf{Q})^*] . \end{aligned} \quad (12)$$

However, this is affected by the noise in Fig. 5(b) to give a signal-to-noise ratio that is still poor, and improving that ratio is one of the issues to be addressed in future work.

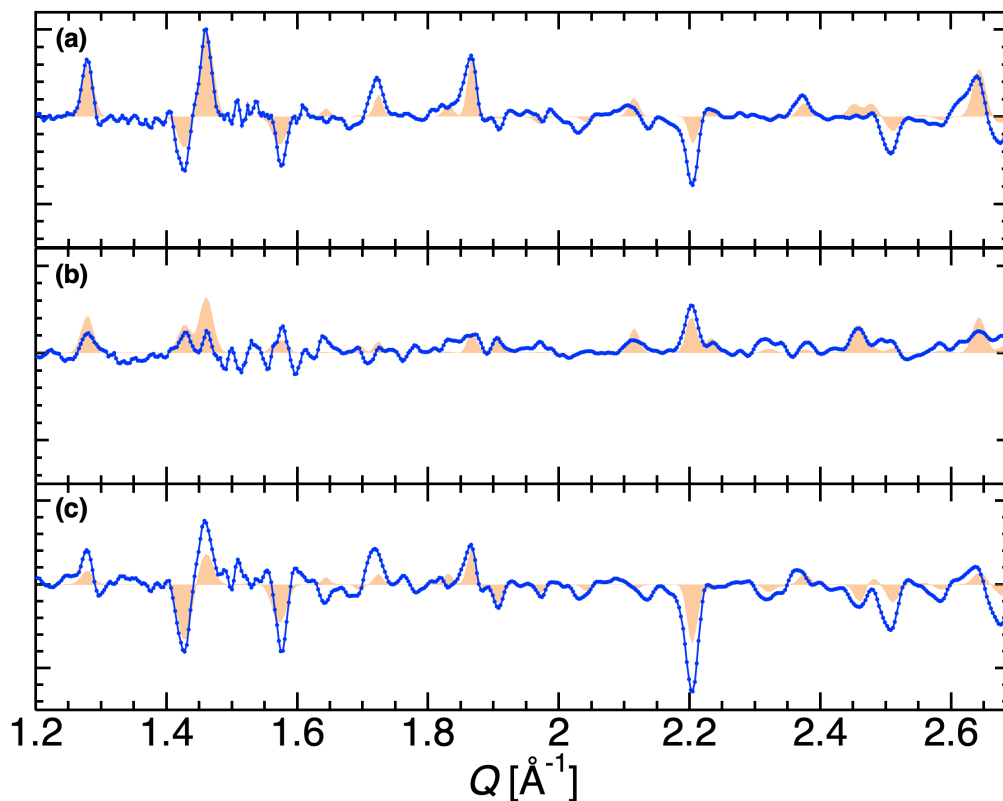


Fig. 5. Blue single-line graphs of (a)  $(m(Q)/Q^2)(|F_H(Q)|^2 + \text{Re}[F_H(Q)F_{\text{others}}(Q)^*])$ , (b)  $(m(Q)/Q^2)|F_H(Q)|^2$ , and (c)  $(m(Q)/Q^2)\text{Re}[F_H(Q)F_{\text{others}}(Q)^*]$  obtained by substituting the experimental data into Eqs. (10), (11), and (12). Orange filled-line graphs are calculated with the peaks broadened by a Gaussian with the resolving power of TAIKAN.

We are now developing a 6.7 T DNP apparatus with wider neutron windows for improved proton polarization,  $Q$  range, and neutron count rates. Measuring at higher proton polarization would give greater differences in peak intensities between different spin configurations, and improved neutron count rates would provide statistical significance in the analysis to determine  $|F_H(Q)|^2$  and  $\text{Re}[F_H(Q)F_{\text{others}}(Q)^*]$ . Although the

opening angle of the neutron windows of approximately  $120^\circ$  of the new DNP apparatus is smaller than those of  $210^\circ$  (Piegsa *et al.*, 2012) and  $360^\circ$  (Pierce, 2017; Pierce *et al.*, 2019), the pulsed neutron measurements with the new DNP apparatus in J-PARC MLF seamlessly cover the  $Q$ -range up to approximately  $10 \text{ \AA}^{-1}$ . Besides, a  $^3\text{He}$  neutron spin filter that polarizes neutrons with  $\lambda$  less than  $1.0 \text{ \AA}$  was recently developed and installed in a crystal diffractometer whose resolving power is higher than that of TAIKAN (Okudaira *et al.*, 2020). In this way, the SCV-NPD performance will be improved by using this advanced apparatus and a beamline suited for crystallography.

We expect that, like anomalous X-ray diffraction, SCV-NPD can be used to separate overlapping diffraction peaks (Friend *et al.*, 1977; Fuoss *et al.*, 1981; Bazin *et al.*, 2002). SCV-NPD controls the coherent scattering length of hydrogen, the main component of soft materials, whereas the X-rays near the absorption edges of light elements cannot be used for scattering measurements. The signal can be separated because of the changing shape and shifting of diffraction peaks due to  $P_{\text{H}}$ . It will be useful for elucidating hydrogen-containing crystals, such as ice systems (Komatsu *et al.*, 2020), polymers (Grishkewich *et al.*, 2017), inorganics (Yashima *et al.*, 2014), and biomacromolecules (Kovalevsky *et al.*, 2008).

We also expect SCV-NPD to be used for studying hydrogen functional materials such as hydrogen storage materials. Compared with hydrogen atoms chemically bounds to specific atoms in organic crystals, those in hydrogen functional materials disperse or flocculate after diffusing among trapping sites, thereby making it difficult to assume the model structures. In SCV-NPD, even if the structure of the sample is unknown, the dispersion and flocculation of hydrogen are determined from  $|F_{\text{H}}(\mathbf{Q})|^2$  and the trapping sites are determined from  $\text{Re}[F_{\text{H}}(\mathbf{Q})F_{\text{others}}(\mathbf{Q})^*]$ .

Whereas SCV-NPD was realized by relayed-DNP in this study, this technique still

has several problems to be solved. For example, the dispersion media produces broad diffraction peaks which overlap with peaks of crystalline domains (See Fig.S2). To overcome the problems, we are planning to use porous polymer materials as the dispersion media. Recently, a dry hydrogel with a volume filling ratio of only 2% (Sekine *et al.*, 2020) has been successfully polarized. We hope that the dispersion media-free sample preparation method will be applied to SCV-NPD.

## 5. Conclusion

We have demonstrated SCV-NPD measurements of LGA using the relayed-DNP technique. With increasing  $P_H$ , some diffraction peaks increased in intensity while the others decreased, and the increasing and decreasing ratios were different for each peak. The structure factor of hydrogen was extracted from the  $P_H$  dependence of the diffraction intensities without assuming structure models. SCV-NPD has the potential to contribute to determining the complicated structures of soft materials whose diffraction peaks cannot be separated or assigned with conventional measurements. In particular, this technique could be used to determine the dispersion, flocculation, and trapping sites of hydrogen atoms in hydrogen functional materials. To improve the performance of the SCV-NPD measurements, we are developing new experiments using a new DNP apparatus with a higher magnetic field, a wider window, and a  $^3\text{He}$  neutron polarizer at the neutron diffractometer for crystallography, a sample preparation using dispersion media with low volume filling ratio, and so on.

### Acknowledgements

The authors would like to thank Dr. M. Kofu of JAEA, Dr. T. Ishida of JFE Steel Corporation, and Dr. K. Ikeda of the High Energy Accelerator Research Organization for their generous support in crystallography and diffractometry measurements. Neutron diffractometry measurements were conducted as part of proposal Nos. 2018P0202,

2019P0202, and 2020P0202 at the J-PARC MLF.

#### Funding information

This work was supported by the Ministry of Education, Culture, Sports, Science and Technology, Japan (grant Nos. 15K04706 and 18K11926) and Grant-in-Aid for Japan Society for the Promotion of Science Fellows 19J23744.

#### References

- Abragam, A., Borghini, M., Catillon, P., Coustham, J., Roubeau, P. & Thirion, J. (1962). *Phys. Lett.* **2**(7), 310 – 311.
- Abragam, A. & Goldman, M. (1978). *Rep. Prog. Phys.* **41**(3), 395–467.
- Bazin, D., Guczi, L. & Lynch, J. (2002). *Applied Catalysis A: General*, **226**(1), 87 – 113.
- Borghini, M. (1966). *CERN Yellow Report*, **66-3**, 28.
- Downs, R. T. & Hall-Wallace, M. (2003). *American Mineralogist*, **88**, 247–250.
- Dunitz, J. D. & Schweizer, W. B. (1995). *Acta Cryst. C*, **51**(7), 1377–1379.
- Friend, R. H., Beal, A. R. & Yoffe, A. D. (1977). *Phil. Mag. A*, **35**(5), 1269–1287.
- Fuoss, P. H., Eisenberger, P., Warburton, W. K. & Bienenstock, A. (1981). *Phys. Rev. Lett.* **46**, 1537–1540.
- Goertz, S. T., Harmsen, J., Heckmann, J., Heß, C., Meyer, W., Radtke, E. & Reicherz, G. (2004). *Nucl. Instrum. Methods. Phys. Res. A*, **526**, 43–52.
- Gražulis, S., Chateigner, D., Downs, R. T., Yokochi, A. F. T., Quirós, M., Lutterotti, L., Manakova, E., Butkus, J., Moeck, P. & Le Bail, A. (2009). *J. Appl. Crystallogr.* **42**(4), 726–729.
- Gražulis, S., Daškevič, A., Merkys, A., Chateigner, D., Lutterotti, L., Quirós, M., Serebryanaya, N. R., Moeck, P., Downs, R. T. & Le Bail, A. (2012). *Nucleic Acids Res.* **40**(D1), D420–D427.
- Grishkewich, N., Mohammed, N., Tang, J. & Tam, K. C. (2017). *Curr Opin Colloid Interface Sc*, **29**, 32 – 45.
- Hayter, J., Jenkin, G. & White, J. (1974). *Phys. Rev. Lett.* **33**(12), 696–699.
- Knop, W., Hirai, M., Olah, G., Meerwinck, W., Schink, H.-J., Stuhrman, H., Wagner, R., Wenkow-EsSouni, M., Zhao, J., Schärpf, O., Crichton, R., Krumpolc, M., Nierhaus, K., Niinikoski, T. & Rijllart, A. (1991). *Physica B Condens. Matter*, **174**(1), 275 – 290.
- Knop, W., Hirai, M., Schink, H.-J., Stuhmann, H. B., Wagner, R., Zhao, J., Schärpf, O., Crichton, R. R., Krumpolc, M., Nierhaus, K. H., Rijllart, A. & Niinikoski, T. O. (1992). *J. Appl. Crystallogr.* **25**(2), 155–165.
- Knop, W., Schink, H.-J., Stuhmann, H. B., Wagner, R., Wenkow-Es-Souni, M., Schärpf, O., Krumpolc, M., Niinikoski, T. O., Rieubland, M. & Rijllart, A. (1989). *J. Appl. Crystallogr.* **22**(4), 352–362.
- Komatsu, K., Machida, S., Noritake, F., Hattori, T., Sano-Furukawa, A., Yamane, R., Yamashita, K. & Kagi, H. (2020). *Nat. Commun.* **11**(1), 464.
- Kovalevsky, A. Y., Katz, A. K., Carrell, H. L., Hanson, L., Mustyakimov, M., Fisher, S. Z., Coates, L., Schoenborn, B. P., Bunick, G. J., Glusker, J. P. & Langan, P. (2008). *Biochemistry*, **2008**(29), 7595–7597.
- Kumada, T., Akutsu, K., Ohishi, K., Morikawa, T., Kawamura, Y., Sahara, M., Suzuki, J.-i. & Torikai, N. (2019). *J. Appl. Crystallogr.* **52**(5), 1054–1060.
- Kumada, T., Noda, Y., Hashimoto, T. & Koizumi, S. (2009). *Physica B Condens. Matter*, **404**(17), 2637–2639.

- Miura, D., Iwata, T., Kaneko, D., Miyachi, Y., Nukazuka, G. & Wauke, H. (2019). *Prog. Theor. Exp. Phys.* **2019**(3). 033D01.
- Momma, K. & Izumi, F. (2011). *J. Appl. Crystallogr.* **44**(6), 1272–1276.
- Niinikoski, T. & Rieubland, J. (1979). *Physics Letters A*, **72**, 141–144.
- Noda, Y., Koizumi, S., Masui, T., Mashita, R., Kishimoto, H., Yamaguchi, D., Kumada, T., Takata, S., Ohishi, K. & Suzuki, J. (2016). *Journal of Applied Crystallography*, **49**(6), 2036–2045.
- Noda, Y., Kumada, T., Hashimoto, T. & Koizumi, S. (2011). *J. Appl. Crystallogr.* **44**(3), 503–513.
- Okudaira, T., Oku, T., Ino, T., Hayashida, H., Kira, H., Sakai, K., Hiroi, K., Takahashi, S., Aizawa, K., Endo, H., Endo, S., Hino, M., Hirota, K., Honda, T., Ikeda, K., Kakurai, K., Kambara, W., Kitaguchi, M., Oda, T., Ohshita, H., Otomo, T., Shimizu, H., Shinohara, T., Suzuki, J. & Yamamoto, T. (2020). *Nucl. Instrum. Methods. Phys. Res. A*, **977**, 164301.
- Piegsa, F., Karlsson, M., van den Brandt, B., Carlile, C., Forgan, E., Hautle, P., Konter, J., Mcintyre, G. & Zimmer, O. (2012). *J. Appl. Crystallogr.* **46**, 30–34.
- Pierce, J. (2017). *Proceedings of science*, **324**, 10.
- Pierce, J., Crow, L., Cuneo, M., Edwards, M., Herwig, K., Jennings, A., Jones, A., Li, L., Meilleur, F., Myles, D., Robertson, L., Standaert, R., Wonder, A. & Zhao, J. (2019). *Nucl. Instrum. Methods. Phys. Res. A*, **940**, 430 – 434.
- Pierce, J., Cuneo J., M., Jennins, A., Li, L., Meilleur, F., Zhao, J. & Myles A.A., D. (2020). *Methods in ENZYMOLOGY*, vol. 643, chap. 8, pp. 153–175. Cambridge, Massachusetts: ACADEMIC PRESS.
- Roinel, Y., Bouffard, V. & Roubeau, P. (1978). *Journal de Physique*, **39**(10), 1097–1103.
- Rossini, A. J., Zagdoun, A., Hegner, F., Schwarzwälder, M., Gajan, D., Copéret, C., Lesage, A. & Emsley, L. (2012). *J. Am. Chem. Soc.* **134**(40), 16899–16908.
- Schmugge, T. J. & Jeffries, C. D. (1965). *Phys. Rev.* **138**, A1785–A1801.
- Sears, V. F. (1992). *Neutron News*, **3**(3), 26–37.
- Sekine, Y., Nankawa, T., Yunoki, S., Sugita, T., Nakagawa, H. & Yamada, T. (2020). *ACS Applied Polymer Materials*, **2**(12), 5482–5491.
- Shibayama, M., Nomura, S., Hashimoto, T. & Thomas, E. L. (1989). *J. Appl. Phys.* **66**(9), 4188–4197.
- Stuhrmann, H. (2004). *Rep. Prog. Phys.* **67**, 1073.
- Takata, S., Suzuki, J., Shinohara, T., Oku, T., Tominaga, T., Ohishi, K., Iwase, H., Nakatani, T., Inamura, Y., Ito, T., Suzuya, K., Aizawa, K., Arai, M., Otomo, T. & Sugiyama, M. (2015). *JPS Conf. Proc.* **8**(036020), 6.
- Tanaka, I., Komatsuzaki, N., Yue, W.-X., Chatake, T., Kusaka, K., Niimura, N., Miura, D., Iwata, T., Miyachi, Y., Nukazuka, G. & Matsuda, H. (2018). *Acta Crystallogr. D*, **74**(8), 787–791.
- van den Brandt, B., Bunyatova, E., Hautle, P., Konter, J. & Mango, S. (1995). *Nucl. Instrum. Methods. Phys. Res. A*, **356**(1), 36 – 38.
- van den Brandt, B., Glattli, H., Grillo, I., Hautle, P., Jouve, H., Kohlbrecher, J., Konter, J., Leymarie, E., Mango, S., May, R., Stuhrmann, H. & Zimmer, O. (2002). *EPL*, **59**, 62–67.
- Yashima, M., Kubo, N., Omoto, K., Fujimori, H., Fujii, K. & Ohoyama, K. (2014). *J. Phys. Chem. C*, **118**(10), 5180–5187.
- Zhao, J., Robertson, L., Herwig, K. & Crabb, D. (2013). *Physics Procedia*, **42**, 39–45.